

Fluorescence Detection of a Trapped Ion with a Monolithically Integrated Single-Photon-Counting Avalanche Diode

W. J. Setzer,^{1, a)} M. Ivory,¹ O. Slobodyan,¹ J. W. Van Der Wall,¹ L. P. Parazzoli,¹ D. Stick,¹ M. Gehl,¹ M. Blain,¹ R. R. Kay,¹ and H. McGuinness¹

Sandia National Laboratories, Albuquerque, New Mexico 87185, USA

(Dated: 5 May 2021)

We report on the first demonstration of fluorescence detection using single-photon avalanche photodiodes (SPADs) monolithically integrated with a microfabricated surface ion trap. The SPADs are positioned below the trapping positions of the ions, and designed to detect 370 nm photons emitted from single $^{174}\text{Yb}^+$ and $^{171}\text{Yb}^+$ ions. We achieve an ion/no-ion detection fidelity for $^{174}\text{Yb}^+$ of 0.99 with an average detection window of 7.7(1) ms. We report a dark count rate as low as 1.2 kHz at room temperature operation. The fidelity is limited by laser scatter, dark counts, and heating that prevents holding the ion directly above the SPAD. We measure count rates from each of the contributing sources and fluorescence as a function of ion position. Based on the active detector area and using the ion as a calibrated light source we estimate a SPAD quantum efficiency of $24\pm 1\%$.

I. INTRODUCTION

Quantum technologies are rapidly advancing with promising applications such as computing and simulation, networking, sensing, and precision timekeeping. However, one of the primary challenges for future quantum devices is the ability to scale up the number of qubits. For ion trap systems, scaling up qubits requires the ability to independently optically address and detect many qubits. Recent work has shown a scalable technology to optically address large numbers of qubits¹⁻⁴, and in this paper, we demonstrate a scalable technology for qubit detection.

A trapped ion's quantum state is typically read out by detecting the fluorescence from a laser driven optical cycling transition. Photon collection efficiency (the fraction of solid angle exposure of the detector to the ion) is typically low and only $\sim 1-2\%$ of emitted photons are collected by optics outside of the vacuum chamber and imaged onto a detector. More light can be collected using higher numerical aperture (NA) optics, however these optics either require short working distances, which interfere with ion trapping, or are prohibitively large and not scalable. External detection readout fidelities at or approaching 0.9999 have been reported with collection efficiencies as high as 10% for optics with $\text{NA} \simeq 0.6^{5-9}$.

Commonly used external detectors for trapped-ion systems, such as photomultiplier tubes (PMT), electron multiplying charge coupled device (EMCCD) cameras, or avalanche photodiode (APD) detectors have quantum efficiencies ranging between 20-40% for blue to UV photons. Superconducting nanowire single photon detectors (SNSPDs), which require cryogenic temperatures for operation, have achieved impressive efficiencies for UV photons as high as 80%^{10,11} and have been used to detect the UV fluorescence from a trapped $^{171}\text{Yb}^+$ qubit with detection fidelities >0.999 in 11 μs ¹². Considering both the collection efficiency and quantum efficiency of the discussed external detectors, the best total detection efficiencies demonstrated range from 2-4%^{9,12}. However, these

demonstrations are not extensible to arbitrarily large arrays of ions, and achieving both scalability and the detection efficiency required for high fidelity state detection remains an ongoing field of research¹³.

A promising solution to the challenge of scalability is to integrate both optical addressing and state read-out on chip. Recently, integrated optical addressing was demonstrated using integrated photonics on a surface trap for the delivery of laser light to trapped ions¹⁻⁴. State read-out has been demonstrated using the several near ion fluorescence collection techniques: optical fibers¹⁴⁻¹⁶, reflective traps^{17,18}, microfabricated optics¹⁹⁻²², and optical cavities²³. For these light collection methods, photon detectors or cameras are still required for detection.

Recently, a SNSPD co-fabricated with a surface-electrode ion trap was used to detect UV light from a $^9\text{Be}^+$ qubit, achieving qubit state readout with fidelity 0.9991(1) in an average of 46 μs ²⁴. It was found that the SNSPD bright counts were reduced by 17% due to the rf fields, even when the SNSPD performance was characterized using low peak amplitude rf, ~ 8 V at 67.03 MHz. For heavier ions like $^{171}\text{Yb}^+$, higher rf peak amplitudes are required for trapping and therefore present a challenge for shielding integrated SNSPD detectors from the higher amplitude rf fields.

In transportable systems, such as atomic clocks, which require lower size, weight, power, and cost (SWaP-C), single-photon avalanche photodiodes (SPADs) provide an alternative path of integrated fluorescence detectors²⁵⁻²⁷ that are compatible with CMOS fabrication and have low dark counts at room temperature²⁸⁻³⁰. Here, we report on the first use of a room temperature surface ion trap that is monolithically integrated with SPADs for measuring ion fluorescence.

II. EXPERIMENTAL SETUP

A SPAD is nominally an APD that is operated in Geiger mode, where it is biased at or beyond its breakdown voltage and extremely sensitive to any charge entering its active area. During a detection event (i.e. a single photon impinging on the active area), the SPAD discharges its built-in over-bias po-

^{a)}Electronic mail: wjsetze@sandia.gov

tential leading to a short dead time depending on the RC feedback of the device. Operation in Geiger mode is necessary for efficient state detection when the photon flux is expected to be low. However it comes at a trade off in terms of the dark count rate (DCR). Dark counts occur when non-photo induced charges that are spontaneously liberated from thermal effects, drift or diffuse into the active area. This results in a false avalanche event that mimics a detection event.

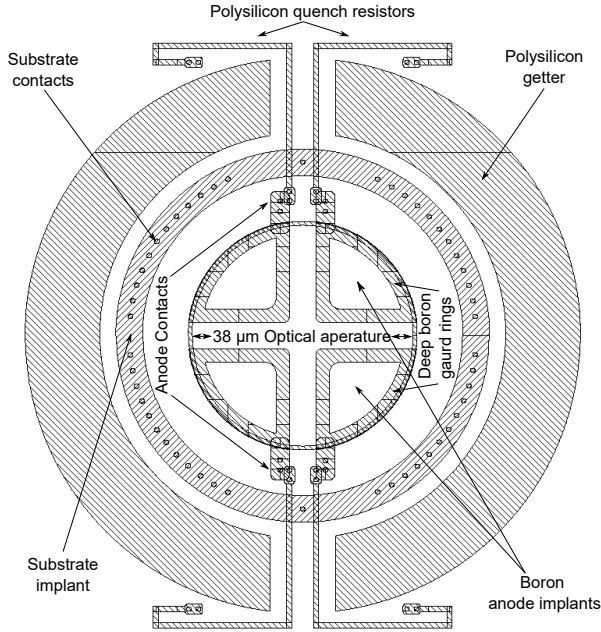


FIG. 1. SPAD schematic showing four quartered SPADs with labeled components. The SPAD anodes are recessed $7 \mu\text{m}$ below the surface of the ion trap within a $38 \mu\text{m}$ diameter optical aperture.

The SPADs, shown in FIG. 1, are designed for compatibility with the trap in their size, film stack-up, and processing. The device is fabricated as a single stack with the SPADs fabricated first. To mitigate risk and test more devices, the circular aperture is split into quarters, each with an independent SPAD. Contacts to the anodes are made using implant tabs that are outside of the optical aperture. Silicon dioxide (SiO_2) thin films above the SPADs which are present during fabrication are later etched away down to an anti reflective coating (ARC) described below.

Edge breakdown in the SPADs is controlled by a deep boron diffused guard ring around the p+ active area perimeter. The deep diffusion reduces the electric field at the device periphery by increasing the radius of the p- region into the epitaxial layer. Without the edge breakdown control the electric field lines would tend to concentrate at the abrupt edge and significantly increase dark counts. As a secondary effect, the guard ring also reduces the effective active area of the device by approximately $2 \mu\text{m}$ from guard ring's inner edge. We determine that this unanticipated effect is due to two mechanisms. First, the deep guard ring requires a high temperature drive-in processing step that causes the dopant to laterally diffuse into the region below the active area. This effectively

extends the width of the guard ring diffusion beyond the intended width. Additionally, the guard ring reduces the vertical electric field near its inner edge, providing some lateral field which does not contribute to avalanche multiplication and results in a reduction in quantum efficiency from the maximum at the device center.

While silicon is strongly absorbing at 370 nm , its large refractive index leads to significant Fresnel reflection ($\sim 57\%$ at normal incidence). For this reason, we deposit an ARC over the SPADs prior to back end deposition of inter-metal dielectric- and metal layers. The ARC layers consists of 10 nm SiO_2 (which also functions as a Si surface passivation layer) followed by a 29 nm layer of silicon nitride. This design is expected to have 10% reflection at normal incidence.

Polysilicon resistors are integrated with the SPADs to quench breakdown events and minimize dead time. The resistors are $1 \mu\text{m}$ wide by $60 \mu\text{m}$ in total length, providing about $300 \text{ k}\Omega$ per resistor. The optical aperture and anodes are surrounded by a substrate contact ring which serves as the cathode contact to the device. Surrounding the substrate contact ring is a $10 \mu\text{m}$ wide ring of polysilicon used as an impurity getter which reduces DCR by collecting mobile impurities (such as metals) that can act as Shockley-Read-Hall generation sites, away from the SPAD junction. The ring is broken at the top and bottom to allow routing of the quench resistors.

To bias the SPADs, the cathode of each SPAD is connected to a shared substrate held at a single voltage. Each individual SPAD's anode is connected to its own detection circuit with a variable offset voltage. For each SPAD, the voltage difference between the offset and substrate determines its bias voltage, allowing control over which SPADs are biased above breakdown. In typical operation, the SPADs are over-biased 4 V above their 28 V breakdown voltage, with 32 V difference between their terminals. SPAD pulses are amplified and filtered by a detection circuit to remove parasitic pickup of the rf drive frequency and are converted to digital pulses by a Schmitt-trigger comparator. The resulting digital pulses are counted and timestamped with $<1 \text{ ns}$ resolution.

Oscilloscope traces acquired before digitization in the detection circuit with the trap rf and lasers off are shown in FIG. 2. Typical pulses at 32 V bias operation have $100\text{--}500 \text{ mV}$ amplitudes and $\sim 1 \mu\text{s}$ duration. Some parasitic pickup of the trap rf still remains after filtering and contributes to dark counts during digitization. An analysis of SPAD pulses with and without trap rf indicates that the trap rf does not contribute additional pulses due to rf heating.

The dark counts of 12 individual SPADs housed within three different optical apertures on the same surface trap are measured in situ; dark counts vary greatly between SPADs, even between those within the same optical aperture, ranging from 1.2 kHz to 140 kHz , with 6 SPAD's having DCR below 10 kHz . Contamination during fabrication has been identified as a possible source for variation in DCR, although defects or metal contamination of the epitaxial Si cannot be ruled out.

We perform spot test measurements to determine the active area of the SPAD detectors, accounting for the guard ring's effect of diminishing the efficiency of bordering SPAD active

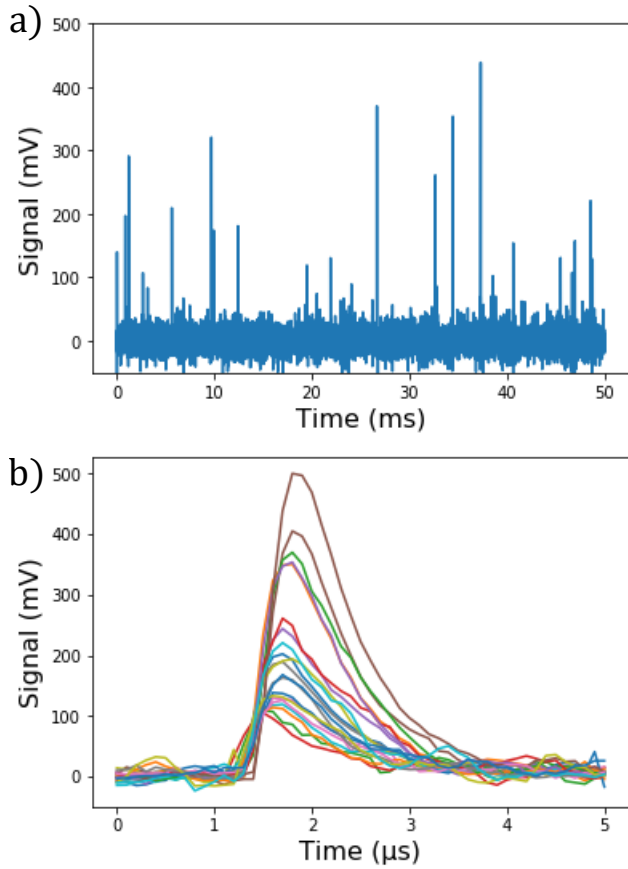


FIG. 2. SPAD pulses. (a) SPAD pulses probed before the Schmitt-trigger comparator in the detection circuit. (b) Stacked pulses from the 50 ms window above. Pulse amplitudes vary with overbias voltage and in typical operation range from 100–500 mV with $\sim 1 \mu\text{s}$ duration.

area, which is particularly important for these quartered detectors as the area is small to begin with. These measurements are accomplished by focusing 370 nm light to a spot diameter of $\sim 1.6 \mu\text{m}$. The spot is scanned in 800 nm steps over the region of the SPAD. An example of the data collected from this procedure is shown in FIG. 3a. To ensure the optical aperture does not interfere with this tight beam we carry this measurement out with devices that have only been fabricated up through the SPAD layers.

For a single quartered SPAD, we determine its active area to be $60 \mu\text{m}^2$. As can be seen in FIG. 3a, the active area of the SPAD is non-uniform, mostly due to the guard ring’s influence. The effective active area is then determined by normalizing the SPAD area to its peak response and calculating the response-weighted surface area over the SPAD region. FIG. 3b shows an SEM image of the SPADs within the optical aperture. At the edge of the optical aperture, the $\sim 1.3 \mu\text{m}$ metal layers are visible with $\sim 1 \mu\text{m}$ SiO_2 layers hidden between them.

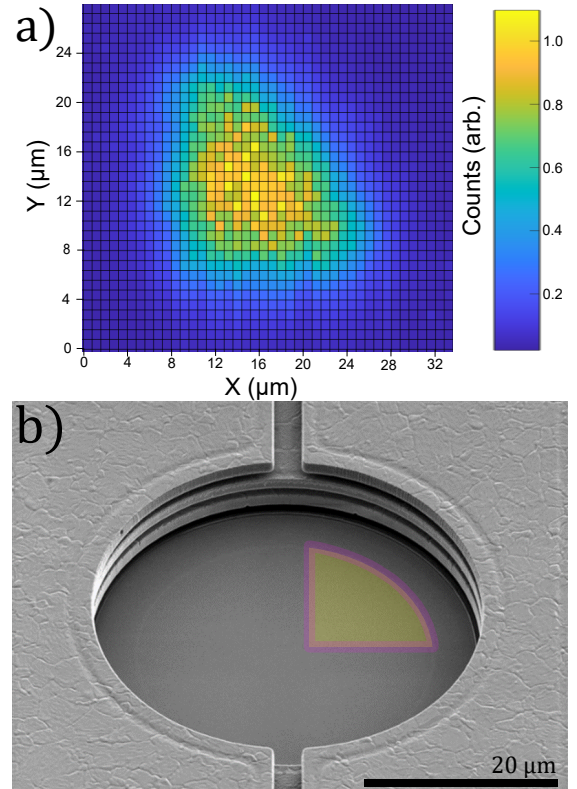


FIG. 3. SPAD active area. (a) Spot test measurements showing the $60 \mu\text{m}^2$ active area of a single quartered SPAD, reduced due to the deep boron guard ring. (b) SEM image of the SPAD detector. False coloring indicates the active area (yellow) and the deep boron guard ring (purple) for one of the four quartered SPADs.

III. EXPERIMENTAL RESULTS

We detect 370 nm fluorescence from the $^2S \leftrightarrow ^2P_{1/2}$ optical cycling transition of the Yb ion. In addition, a 935 nm repump laser is needed to de-populate a long-lived state using the $^2D_{3/2} \leftrightarrow ^3[3/2]_{1/2}$ transition. We have successfully trapped and detected fluorescence from $^{171}\text{Yb}^+$, however it has a lower fluorescence rate due to coherent population trapping³¹ so we use $^{174}\text{Yb}^+$ to characterize the SPADs. The lack of hyperfine structure in $^{174}\text{Yb}^+$ makes qubit state preparation and detection difficult, so we have left integrated qubit state detection for future work.

A false color SEM image of the surface trap with integrated SPADs used in this experiment is shown in FIG. 4. The trap is housed in a UHV chamber with operating pressures below 1×10^{-11} Torr. The rf electrodes indicated in blue provide confinement along the trap axis $50 \mu\text{m}$ above the trap surface. The DC electrodes indicated in green allow for ion shuttling along the rf null. Ions are loaded at loading slots (example location indicated by the red circle in FIG. 4) and shuttled toward the detector. A magnetic field of 5 Gauss is applied perpendicular to the plane of the trap surface to lift the degeneracy between $^{171}\text{Yb}^+$ hyperfine sub-levels and provide a quantization axis for beam polarizations.

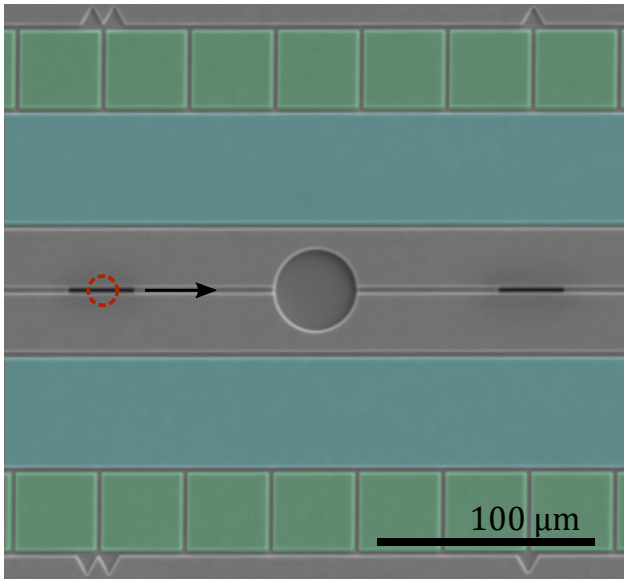


FIG. 4. SEM image of the ion trap with integrated SPADs. False color has been added to indicate the rf electrodes (blue) and DC electrodes (green). Ions are loaded above the slot indicated by the red circle and trapped $50 \mu\text{m}$ above the trap surface. Ions are then shuttled along the trap axis towards the SPAD indicated by the black arrow.

TABLE I. Count Budget

Source	Counts (kHz)
Ion Fluorescence	4.8
935 nm Repump Scatter	4.0
370 nm Doppler Scatter	1.4
Dark Counts	1.2
rf Pickup	0.3

This field had no discernible impact on SPAD performance. An rf drive frequency of 17.7 MHz with peak amplitude below 30 V on the RF electrodes results in typical motional frequencies of $2\pi \times 1.3\text{--}2.0$ MHz in the radial directions and an axial frequency of $\sim 2\pi \times 450$ kHz. These frequencies are verified via spectroscopy on the $|2S_{1/2}, F=0, m_F=0\rangle$ to $|2D_{3/2}, F=2, m_F=+2\rangle$ $^{171}\text{Yb}^+$ quadrupole clock transition.

Even without powering the SPADs, the ions were motionally excited, which prevented sideband cooling and heating rate measurements. We tested a gold coated device and found similar motional excitation, indicating that this heating has other causes such as low motional frequencies or uncompensated axial micromotion. We also observe ion heating due to SPAD pulses when the SPADs are biased above breakdown, however the heating per pulse could not be quantified and therefore will need to be investigated in a future device.

The SPAD counts for a typical detection experiment are shown in Table I. The count budget is acquired by toggling beams and the trap rf after the ion has been removed from the trap. In typical freespace imaging systems a filter is used to block scattered light from the 935 nm repump laser from

reaching the detector. For our integrated detector this is not possible. Therefore, laser scatter is minimized by adjusting the position, focus, and intensity of the beams. Despite minimization, scattered laser light remained the dominant source of non-ion counts. There is a trade-off between ion fluorescence and laser beam intensity; for the data shown the beam intensities were lowered until the ions were held at $\sim 83\%$ of saturation fluorescence to minimize laser scatter while maximizing fluorescence. The rf counts result from parasitic pickup will likely be reduced in the future with improved filtering and shielding.

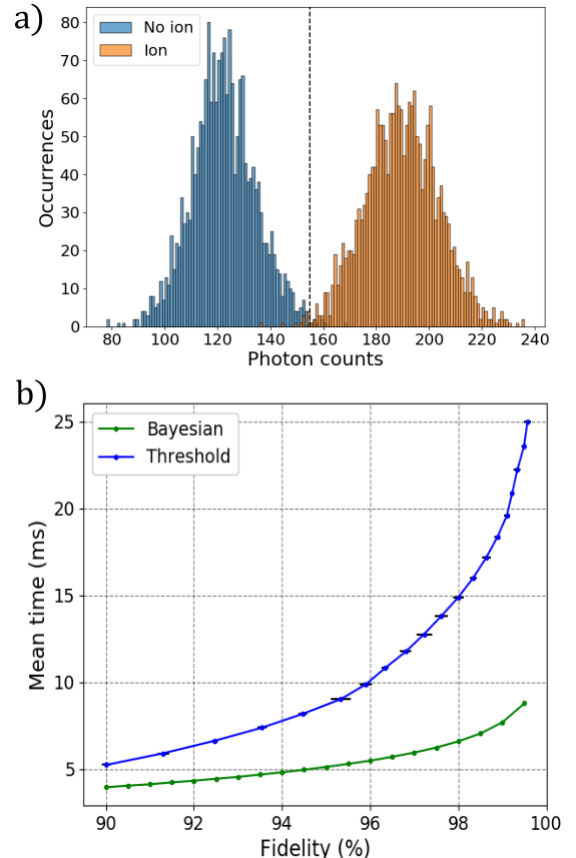


FIG. 5. Detection Fidelity. (a) Ion/No-ion count histogram generated using a 24.5 ms detection window and repeated over 50 s before (orange) and after removing the ion from the trap (blue). The dashed line indicates the threshold for optimal fidelity of 0.995(1). (b) Fidelity plot showing average gate time to reach a target fidelity using the standard thresholding (blue) and adaptive Bayesian technique (green). Using the adaptive Bayesian technique we measure an ion/no-ion fidelity of 0.99 with an average detection window of 7.7(1) ms.

To characterize the ion/no-ion detection fidelity, digitized pulses from a single quartered SPAD are timestamped for 50 s before and after removing the ion from the trap. The resulting timestamped datasets are then gated, counted, and binned to generate ion/no-ion count histograms. An example count histogram generated using a 24.5 ms gate is shown in FIG. 5a. With the timestamp datasets we have analyzed the ion/no-ion detection fidelity using both the standard threshold technique

and an adaptive Bayesian technique that allows for a variable gate time to achieve a target fidelity^{5,24,32}. Using the latter technique, we measure the presence of an ion with 99% accuracy, within an average detection window of 7.7(1) ms, as shown in FIG. 5b.

With the SPADs biased below breakdown an ion can be shuttled directly above the center of the SPAD's optical aperture. However, above the breakdown voltage SPAD pulses heat the ion out of the trap indicating the need for additional electric field shielding, such as a mesh or indium tin oxide (ITO) coating. The SPADs are recessed 7 μm below the metal surface of the trap which provides additional shielding of the ion the further it is away from the center of optical aperture. This lack of shielding limits fluorescence data collection to lateral ion positions greater than 68 μm from the center of the SPAD's aperture.

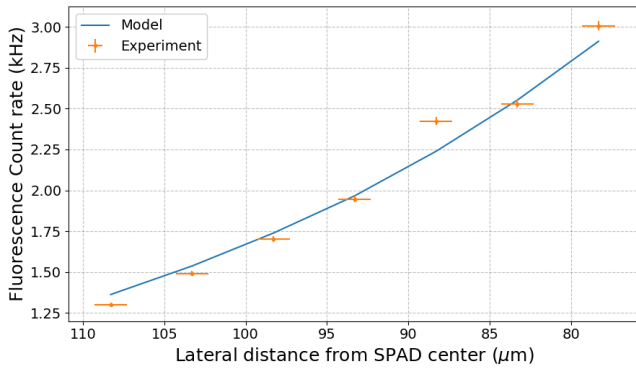


FIG. 6. Collection Efficiency. The fluorescence collection efficiency of the detector is modeled using the SPAD's 60 μm^2 active area (blue curve). Experimental fluorescence counts are gathered as the ion incrementally shuttled closer to the SPAD in 5 μm lateral steps (orange points).

The collection efficiency of a single quartered SPAD is modeled using the fraction of fluorescence solid angle emission incident on the 60 μm^2 active area, accounting for the loss from the ARC. As the angle of incidence increases, the anti-reflection minimum shifts to shorter wavelengths, leading to an increase in reflected light at 370 nm. The results of this model are shown in FIG 6 as the blue curve. This collection efficiency is verified experimentally by collecting count data while incrementally shuttling the ion closer to the SPAD in 5 μm lateral steps along the trap axis. Fluorescence counts at each shuttling location are acquired by subtracting average ion and no-ion counts using 30 ms gating of 50 s ion/no-ion datasets (orange points in FIG 6). The collection efficiency ranges from 0.03% at 80 μm from the SPAD center to 0.14% if the ion were directly over the SPAD. Most of this can be explained by the reduction in active area due to quartering the SPAD; if it were not quartered the collection efficiency would increase from 0.14% to 2.6%. We estimate that for a square SPAD that encompasses the entire width between the RF electrodes, 10% collection efficiencies could be achieved.

Fluorescence is monitored during shuttling with our free-space imaging system and kept constant to $\sim 83\%$ of saturation fluorescence by adjusting laser beam positions. The

$^{174}\text{Yb}^+$ linewidth, $\gamma/2\pi = 19.6$ MHz, along with the our modeled collection efficiency gives an expected incident photon rate for each ion shuttling position. The ratio of expected incident photons to the measured fluorescence counts is fit with a single parameter to give a quantum efficiency of the SPAD of $24 \pm 1\%$. The reflection from the ARC ranges from 22.5% to 17.3% reflected light over the shuttling range shown and as low as 10% at normal incidence. Additional shielding, allowing for closer ion proximity to the detector, will significantly improve collection efficiency.

IV. CONCLUSION

We have demonstrated ion trapping and fluorescence detection in a surface trap with monolithically integrated SPAD detectors. This is the first detection of a trapped ion at room temperature using trap integrated detectors. We measure a quantum efficiency of $24 \pm 1\%$ with detector dark counts as low as 1.2 kHz and detect the presence of an ion with 99% fidelity, within an average detection window of 7.7(1) ms using an adaptive Bayesian method. This fidelity is limited primarily by detector dark counts, laser scatter, and limited ion proximity due to heating from SPAD voltage pulses. We expect material improvements to reduce dark counts and the variability between SPADs, and optical filters can be microfabricated to reject light from sources at other wavelengths. An order of magnitude increase in collection efficiency may be achieved using a larger single SPAD and placing the ion directly over the detector, which relies on electrically screening the ion from the SPAD. If these improvements were made with the same quantum efficiency (24%) and dark count rate (1.2 kHz) measured here, the device could achieve $>99.9\%$ state detection fidelity in 50 μs . We believe these trap-integrated detection results are a significant step towards the scalability and deployability of future atom-chip quantum technologies.

V. ACKNOWLEDGMENTS

The authors thank the members of Sandia's Microsystems and Engineering Sciences Application (MESA) facility for their fabrication expertise for helpful comments on the manuscript. This work was supported by the Defense Advanced Research Projects Activity (DARPA). Sandia National Laboratories is a multi-mission laboratory managed and operated by National Technology & Engineering Solutions of Sandia, LLC, a wholly owned subsidiary of Honeywell International Inc., for the U.S. Department of Energy's National Nuclear Security Administration under contract DE-NA0003525. This paper describes objective technical results and analysis. Any subjective views or opinions that might be expressed in the paper do not necessarily represent the views of the U.S. Department of Energy or the United States Government.

¹K. K. Mehta, C. D. Bruzewicz, R. McConnell, R. J. Ram, J. M. Sage, and J. Chilverini, Nature Nanotechnology **11**, 1066 (2016).

- ²R. J. Niffenegger, J. Stuart, C. Sorace-Agaskar, D. Kharas, S. Bramhavar, C. D. Bruzewicz, W. Loh, R. T. Maxson, R. McConnell, D. Reens, G. N. West, J. M. Sage, and J. Chiaverini, *Nature* **586**, 538 (2020).
- ³K. K. Mehta, C. Zhang, M. Malinowski, T.-L. Nguyen, M. Stadler, and J. P. Home, *Nature* **586**, 533 (2020).
- ⁴M. Ivory, W. J. Setzer, N. Karl, H. McGuinness, C. DeRose, M. Blain, D. Stick, M. Gehl, and L. P. Parazzoli, “Integrated optical addressing of a trapped ytterbium ion,” (2020), arXiv:2011.12376 [quant-ph].
- ⁵A. H. Myerson, D. J. Szwer, S. C. Webster, D. T. C. Allcock, M. J. Curtis, G. Imreh, J. A. Sherman, D. N. Stacey, A. M. Steane, and D. M. Lucas, *Phys. Rev. Lett.* **100**, 200502 (2008).
- ⁶A. H. Burrell, D. J. Szwer, S. C. Webster, and D. M. Lucas, *Phys. Rev. A* **81**, 040302 (2010).
- ⁷J. E. Christensen, D. Hucul, W. C. Campbell, and E. R. Hudson, *npj Quantum Information* **6** (2020), 10.1038/s41534-020-0265-5.
- ⁸L. A. Zhukas, P. Svihra, A. Nomerotski, and B. B. Blinov, “High-fidelity simultaneous detection of trapped ion qubit register,” (2020), arXiv:2006.12801 [quant-ph].
- ⁹R. Noek, G. Vrijsen, D. Gaultney, E. Mount, T. Kim, P. Maunz, and J. Kim, *Opt. Lett.* **38**, 4735 (2013).
- ¹⁰D. H. Slichter, V. B. Verma, D. Leibfried, R. P. Mirin, S. W. Nam, and D. J. Wineland, *Opt. Express* **25**, 8705 (2017).
- ¹¹E. E. Wollman, V. B. Verma, A. D. Beyer, R. M. Briggs, B. Korzh, J. P. Allmaras, F. Marsili, A. E. Lita, R. P. Mirin, S. W. Nam, and M. D. Shaw, *Opt. Express* **25**, 26792 (2017).
- ¹²S. Crain, C. Cahall, G. Vrijsen, E. E. Wollman, M. D. Shaw, V. B. Verma, S. W. Nam, and J. Kim, *Communications Physics* **2** (2019), 10.1038/s42005-019-0195-8.
- ¹³C. D. Bruzewicz, J. Chiaverini, R. McConnell, and J. M. Sage, *Applied Physics Reviews* **6**, 021314 (2019), <https://doi.org/10.1063/1.5088164>.
- ¹⁴C. R. Clark, C.-w. Chou, A. R. Ellis, J. Hunker, S. A. Kemme, P. Maunz, B. Tabakov, C. Tigges, and D. L. Stick, *Phys. Rev. Applied* **1**, 024004 (2014).
- ¹⁵H. Takahashi, A. Wilson, A. Riley-Watson, F. Oručević, N. Seymour-Smith, M. Keller, and W. Lange, *New Journal of Physics* **15**, 053011 (2013).
- ¹⁶A. P. VanDevender, Y. Colombe, J. Amini, D. Leibfried, and D. J. Wineland, *Phys. Rev. Lett.* **105**, 023001 (2010).
- ¹⁷P. F. Herskind, S. X. Wang, M. Shi, Y. Ge, M. Cetina, and I. L. Chuang, *Opt. Lett.* **36**, 3045 (2011).
- ¹⁸A. V. Rynbach, P. Maunz, and J. Kim, *Applied Physics Letters* **109**, 221108 (2016).
- ¹⁹J. T. Merrill, C. Volin, D. Landgren, J. M. Amini, K. Wright, S. C. Doret, C.-S. Pai, H. Hayden, T. Killian, D. Faircloth, K. R. Brown, A. W. Harter, and R. E. Slusher, *New Journal of Physics* **13**, 103005 (2011).
- ²⁰M. Ghadimi, V. Blüms, B. G. Norton, P. M. Fisher, S. C. Connell, J. M. Amini, C. Volin, H. Hayden, C.-S. Pai, D. Kielpinski, M. Lobino, and E. W. Streed, *npj Quantum Information* **3** (2017), 10.1038/s41534-017-0006-6.
- ²¹A. Jechow, E. W. Streed, B. G. Norton, M. J. Petrusianas, and D. Kielpinski, *Opt. Lett.* **36**, 1371 (2011).
- ²²E. W. Streed, B. G. Norton, A. Jechow, T. J. Weinhold, and D. Kielpinski, *Phys. Rev. Lett.* **106**, 010502 (2011).
- ²³J. D. Sterk, L. Luo, T. A. Manning, P. Maunz, and C. Monroe, *Phys. Rev. A* **85**, 062308 (2012).
- ²⁴S. L. Todaro, V. B. Verma, K. C. McCormick, D. T. C. Allcock, R. P. Mirin, D. J. Wineland, S. W. Nam, A. C. Wilson, D. Leibfried, and D. H. Slichter, *Phys. Rev. Lett.* **126**, 010501 (2021).
- ²⁵K. K. Mehta, *Integrated optical quantum manipulation and measurement of trapped ions*, Ph.D. thesis, Massachusetts Institute of Technology (2017).
- ²⁶G. N. West, *Visible and ultraviolet integrated photonics for addressing atomic systems*, Ph.D. thesis, Massachusetts Institute of Technology (2019).
- ²⁷M. K. Ivory, M. Gehl, W. J. Setzer, H. J. E. McGuinness, R. A. Haltli, M. G. Blain, D. L. Stick, and L. P. Parazzoli, “Tictoc: Compact atomic clock with integrated photonics.” (2019).
- ²⁸D. Bronzi, F. Villa, S. Bellisai, B. Markovic, S. Tisa, A. Tosi, F. Zappa, S. Weyers, D. Durini, W. Brockherde, and U. Paschen, in *2012 Proceedings of the European Solid-State Device Research Conference (ESSDERC)* (2012) pp. 230–233.
- ²⁹D. Bronzi, F. Villa, S. Bellisai, S. Tisa, A. Tosi, G. Ripamonti, F. Zappa, S. Weyers, D. Durini, W. Brockherde, and U. Paschen, in *Quantum Sensing and Nanophotonic Devices X*, Vol. 8631, edited by M. Razeghi, International Society for Optics and Photonics (SPIE, 2013) pp. 241 – 248.
- ³⁰C. Veerappan and E. Charbon, *IEEE Transactions on Electron Devices* **63**, 65 (2016).
- ³¹S. Ejtemaee, R. Thomas, and P. C. Haljan, *Phys. Rev. A* **82**, 063419 (2010).
- ³²D. B. Hume, T. Rosenband, and D. J. Wineland, *Phys. Rev. Lett.* **99**, 120502 (2007).